J. Earth Syst. Sci. (2023)132 107
https://doi.org/10.1007/s12040-023-02119-9

Comparison of the pyGIMLi and BERT packages for landslide and cavity detection: A case study from Tghat-Oued Fez, Morocco

Oussama Jabrane[1,*], Driss El Azzab[1], Pedro Martínez-Pagán[2], Mohammed Charroud[1], Bouabid El Mansouri[3], Marcos A Martínez-Segura[2], Mahjoub Himi[4] and Mohammed Elgettafi[5]

[1] *Faculty of Science and Technology, SIGER Laboratory, Sidi Mohamed Ben Abdellah University, BP 2202, Fez, Morocco.*
[2] *Department of Mining and Civil Engineering, Universidad Politecnica de Cartagena, Paseo Alfonso XIII, 52, 30203 Cartagena, Spain.*
[3] *Faculty of Science, LGRN Laboratory, Ibn Toufail University, BP 133, 1400 Kenitra, Morocco.*
[4] *Departament de Minerologia Petrologia i Geologia Aplicada, Universitat de Barcelona, Barcelona, Spain.*
[5] *Polydisciplinary Faculty of Nador, LCM2E Lab Géo-Environnement et Santé, Mohamed First University, BP 300, 26702 Selouane, Morocco.*
* *Corresponding author. e-mail: jabraneoussama@gmail.com oussama.jabrane@usmba.ac.ma*

MS received 4 November 2022; revised 16 January 2023; accepted 22 March 2023

In the present study, two-dimensional (2D) electrical resistivity tomography (ERT) and vertical electrical sounding (VES) techniques were adopted to predict and detect landslides and subsurface voids occurrences in the Tghat-Oued Fez district of Fez city, Morocco. The purpose of this research is to examine the effects of electrical-based applied geophysics methods for data inversion and modelling using open-source algorithms for spatial distribution and shape of sliding and underground cavities as well as fractured zones in the study area. The data acquisition was based on nine ERT profiles using a dipole–dipole electrode array configuration and 72 VES soundings laid out on an area in which underground cavities were expected. 2D electrical sections, derived from electrical resistivity tomography measurements, in terms of electrical resistivity contrast, correctly highlighted the site's well-defined lithology, identified the presence of cavities with variable geometry, and were capable of inferring the sliding surface. VES-based measurements, in conjunction with the ERT technique, mapped the potential presence of near-surface voids inside a conductive marly formation caused by high electrical resistivity anomalies and delimited the conglomerate roof layer. The joint combination of these two electrical-based geophysical methods along with the numerical modelling and inversion of the data structure and parameters using the useful features of the open-source python-based environment pyGIMLi and BERT, have demonstrated their capability to infer near-surface voids in the study area. The geophysical survey results suggest that the integrated geophysical approach is a reliable and capable geophysical tool and could be effectively used for landslide, and cavity detection and to assess the risk of those subsidence-prone areas. Thus, this approach could be easily applied and reproduced in those areas with similar characteristics.

Keywords. ERT; VES; landslide detection; near-surface voids; pyGIMLi; BERT; Fez; Morocco.

---

1. Introduction

Geophysical methods have wide applications in engineering and environmental investigations, mineral exploration, and tectonics (Ward 1990a, b; Gambetta *et al.* 2011; Essa *et al.* 2020, 2021; Kumar *et al.* 2021, 2022; Gan *et al.* 2022; Mehanee 2022a). Landslides and underground cavities pose a major concern for land use and urban planning. Those cavities can be empty, full, or partly water-filled or filled with sediments (Van Schoor 2002; Zhou *et al.* 2002; Gómez-Ortiz and Martín-Crespo 2012; Plank and Polgár 2019; Fu *et al.* 2020; Arjwech *et al.* 2021; Boualla *et al.* 2021). Sub-surface or near-surface, sliding, and voids can cause disturbances in construction works and constitute a potential risk during and after infrastructure projects. Not to mention the increase in working costs and delays. Subsidence and cracking can happen slowly over time, affecting the topography of the surface, which could lead to sudden collapses, presenting a high risk for human safety and infrastructure. Therefore, it is a top priority to detect underground cavities in void-prone urban areas before any construction project could be undergone.

Different prospecting techniques are routinely and successfully conducted to detect landslides and underground voids (Kang *et al.* 2019; Caleb and Anthony 2022). In fact, several examples dealing with the combination of multiple geophysical techniques can be found in the most recent research into this topic. Among them stands out the successful employ of microgravimetry and ground-penetrating radar (Nuzzo *et al.* 2007; Leucci and Giorgi 2010; Gambetta *et al.* 2011; Gómez-Ortiz and Martín-Crespo 2012; Carbonel *et al.* 2015), 2D electrical resistivity tomography (Zhou *et al.* 2002; Göktürkler *et al.* 2008; Gómez-Ortiz and Martín-Crespo 2012; Martínez-Pagán *et al.* 2013; Metwaly and Al Fouzan 2013; Whiteley *et al.* 2019; Boualla *et al.* 2021), magnetometry (Gibson *et al.* 2004; Putiska *et al.* 2014; Hasan *et al.* 2020; Mehanee *et al.* 2021), 1D and 2D inversion of VES (Balkaya *et al.* 2012), and seismic methods (Cook 1965; Grandjean 2006; Cardarelli *et al.* 2010; Ivanov *et al.* 2016; Whiteley *et al.* 2019). Despite those studies, there is still room for further improvement and better knowledge of the true capability of geophysical techniques to determine void occurrences since they are geologic and/or human-induced structures of great concern and where climate change is likely to increase their impact.

The present work has been addressed to assess the capability of electrical-based techniques for cavity detection and landslide monitoring in the northern part of the urban area of Fez, Morocco, whose presence is expected on its northern border. Given its perfect location dominating the city and its spectacular sightseeing, Tghat district is in great demand for new construction and settlement projects. The rapid growth of the population is associated with environmental factors, such as tectonic activity, bedrock lithology, and entropic actions in this area. All these parameters could produce imbalances, which can lead to tragic events.

In such cases, selecting the appropriate geophysical methods for cavities and landslide detection depends on the geological environment, which significantly influences the final choice. In this context, the main aims were: (a) to demonstrate 1D and 2D geoelectrical signal processing for cavity detection and landslide monitoring, as well as to demonstrate the data structure and parameters by utilizing the useful features of the open-source pyGIMLi python environment, (b) to determine the actual capability of electrical-based geophysical techniques to detect near-surface voids in the study area, (c) to evaluate how well VES and ERT techniques interrelate, and (d) to assess the potential use of VES for void identification for those final civil work practitioners with a slight possibility of accessing to more capable techniques such as ERT-based methodologies.

2. Geological setting of the study area

The study area is located at the intersection between the pre-Rif mountains and the Sais Plain. Tghat-Oued Fez district is a small region situated north of Fez city, Morocco, on the southeastern slope of Tghat Mountain (figures 1, 3). The selection of this site was justified because of its void-prone occurrence as well as its excessive urbanization. Those circumstances pose the challenge of integrating those lands into new urban development plans without compromising infrastructure safety. Furthermore, it was possible during this study to identify the occurrence of land subsidence phenomena, microcracks, fissures, and some landslide-prone structures (figure 2). However, knowing the geological nature of the sub-surface is not enough to have an exact idea about void occurrence and its near-surface distribution.

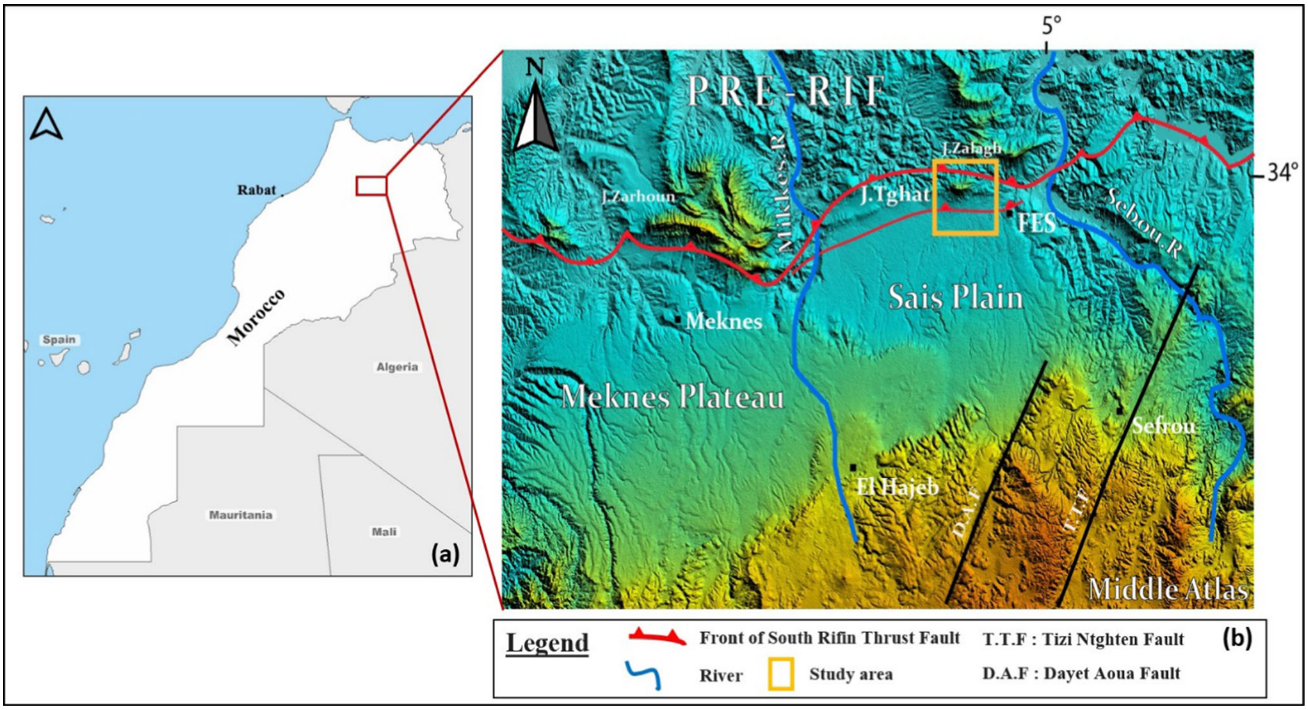

Figure 1. **(a)** The geographical location of the study area (within the red box). **(b)** Digital elevation model (DEM) showing the study area and the main structures of Sais plain.

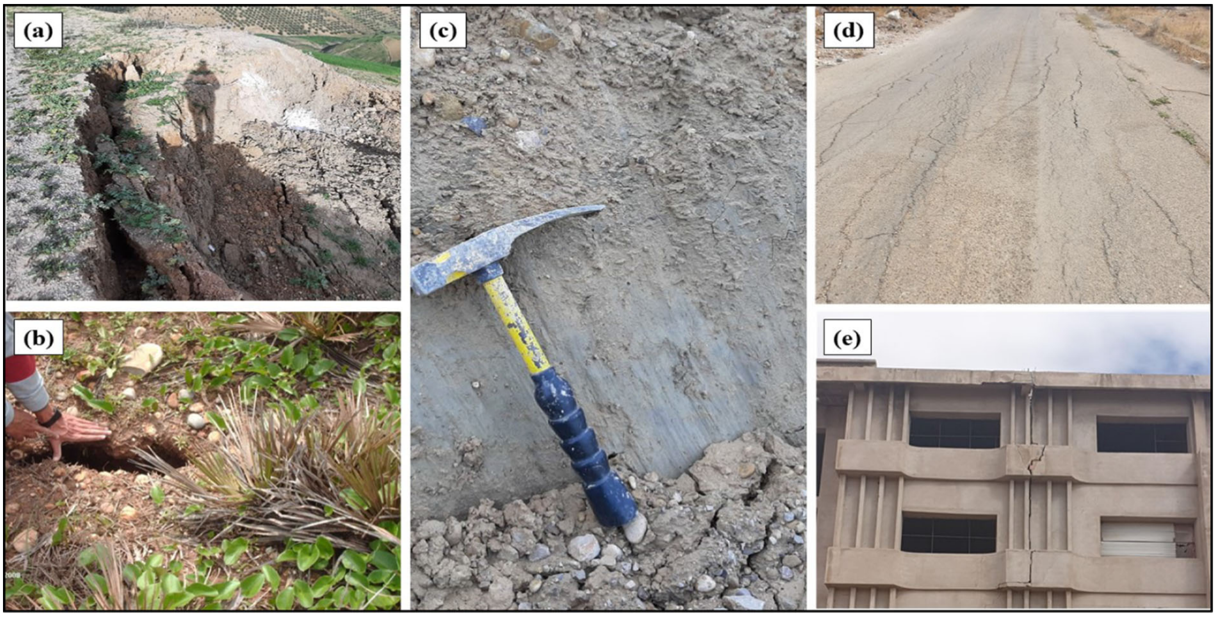

Figure 2. Photographs of different structures exposed in the area. **(a)** Landslide occurrence, **(b)** wide (30 cm) and deep cracks in the glacis deposits, **(c)** fresh sliding surface, **(d)** severe alligator-shaped cracking, and **(e)** visible cracks on new constructions.

The northern edge of the Sais plain corresponds to the Tghat and Zalagh ridges and their annexed branches materializing the South-Rifin Thrust Front (SRF) (figure 3a). These are compressive structures in overlapping ramps on the plain of Fez. This system of ramps, which constitutes the SRF, develops inside the plain of Fez through the structures of Tghat and Sidi Hrazem. The deformation associated with these structures allowed the rising of the endorheic Pliocene basin and the elevation of two ridges of over 500 m above Sais plain (Charroud *et al.* 2006; Cherai *et al.* 2008).

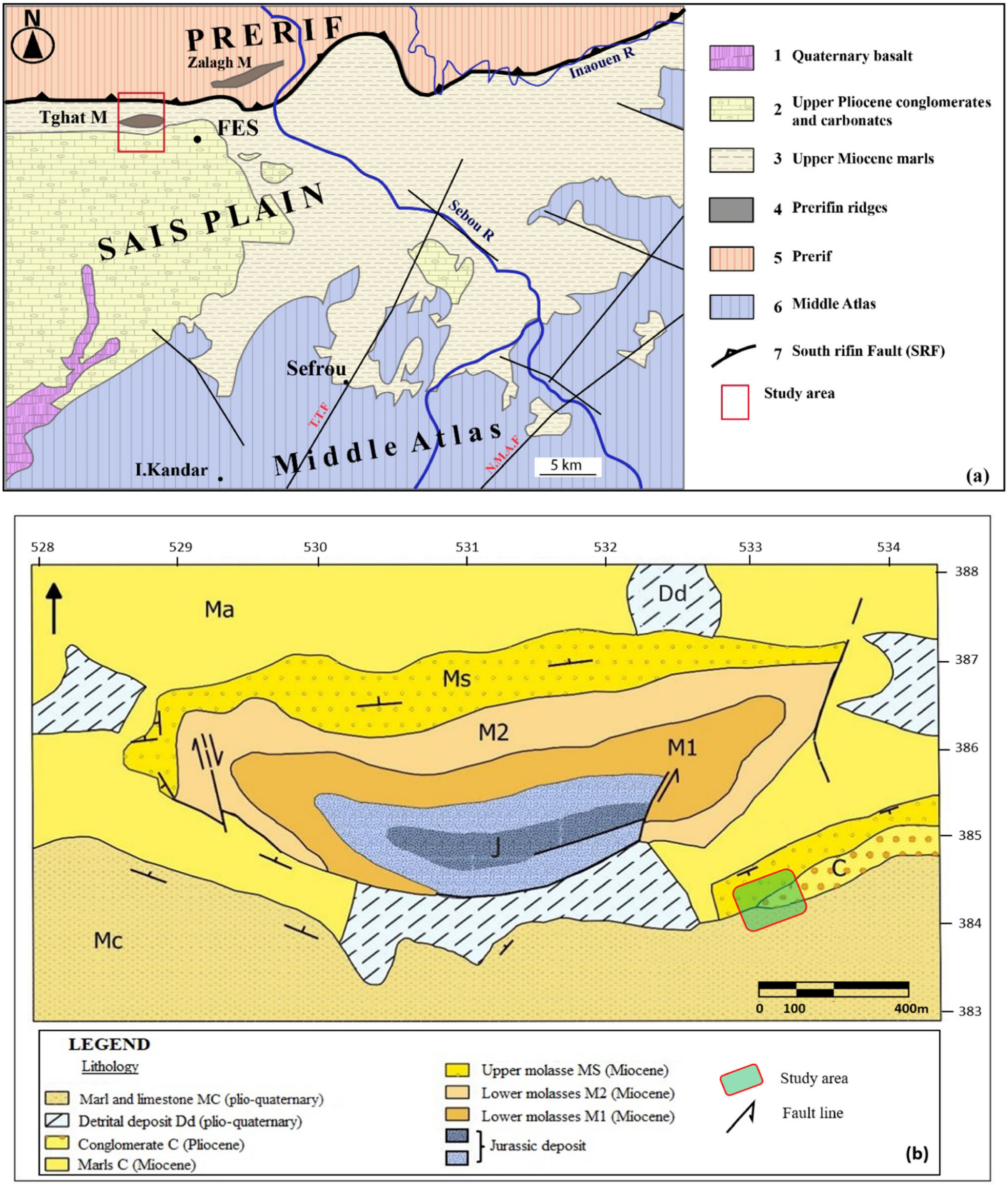

Figure 3. **(a)** Simplified geological map of Eastern Sais plain, and its atlasic and rifin edges and **(b)** Tghat ridge geological map.

The structure of Jbel Tghat (figure 3b) is an elongated relief in an east–west direction, located to the south of the frontal limit of the pre-rifinal complex (Faugeres 1978; Cherai *et al.* 2004; Charroud *et al.* 2006). It is a massif with a Jurassic core and a Miocene cover. That mountain has an altitude of 873 m above sea level, making it strongly straightened and dominates, by nearly 400 m, the plain of Fez located to the south. The Sais Plain evolved from a foreland basin, before the

Miocene, to a continental endorheic basin in the Pliocene and then to a tilted plateau in the Quaternary age. This evolution has produced a variety of deposits whose properties and characteristics depend on their specific environmental origin.

At the base of the Tghat ridge, several deformations were observed within the slope deposits, which constitute evidence of the most recent tectonic activity. This activity, which is evident throughout the northern edge of the Sais Plain, was comprehensibly described in previous works conducted in the study area (Taltasse 1953; Ahmamou *et al.* 1989; Bargach *et al.* 2004; Cherai *et al.* 2004, 2007). The existence of tectonic readjustments, closely associated to the SRF movement, increases the possibility of soil erosion, land subsidence, and landslide phenomena, especially promoted with the presence of cavities in the study area, which could otherwise cause damage to roads and nearby structures.

The study area is mostly characterized by Miocene and Plio-Quaternary deposits (figure 4). The study zone shows three well-defined units, as follows:

Colluvial cover unit: Generally, slope materials, usually present on the southern slope of the study area, forming a fine sub-surface layer. Depending on the location of the deposits the thickness varies from 1 to 4 m. It is a formation composed essentially of rounded elements, pebbles, gravel, and elements of multi-metric Burdigalian sandstones. The origin of this formation comes from the erosion of the upper pudding drowned into a silt-argillaceous and white-clayey-marly matrix.

Marlstone unit: The green to whitish marls of the Oued-Fez deposits, which contain concrete gypsum, reflecting a lacustrine environment with intense evaporation, this formation is described in previous works. It is a homogeneous and compact unit in depth. However, these deposits are sensitive to the presence of water, representing an unstable and slippery formation to the south. The marl layers generally have gentle slopes but, in some places, can be locally steeper (up to 15°). This formation is extremely cracked and presents many fissures on the surface.

Conglomerate unit: A layer formed by detrital terrigenous and siliciclastic materials. This unit is a pudding of mostly decimetric and centimetric subrounded polygenic and polymeric fragments, which are packed in a brown to yellowish-red clay matrix, which is a polygenic conglomerate of probably Liasic and Miocene origin.

3. Methodology

Two electrical-based geophysical methods were applied in the study area: 2D electrical resistivity tomography (ERT) and vertical electrical sounding (VES) techniques. Electrical data were collected from a total of nine ERT profiles and 72 VES soundings (figure 5). As aforementioned, the survey was conducted in an area belonging to the city of Fez, which is affected by cavities and landslides (Charroud *et al.* 2007; Cherai *et al.* 2007, 2008).

Regarding vertical electrical sounding (VES) technique, this is one of the classical direct current (DC) geoelectrical prospecting techniques (Niculescu and Andrei 2019). VES is used to non-invasively retrieve subsurface resistivity variation with depth. To accomplish that objective the electrode spacing (AB for current electrodes, and MN for potential electrodes) interval is changed while

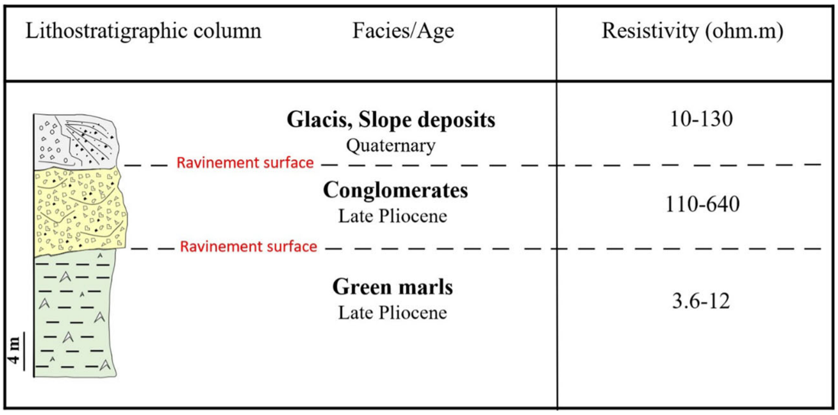

Figure 4. Lithostratigraphic column showing the different geological units present in the study area and their associated electrical resistivity values.

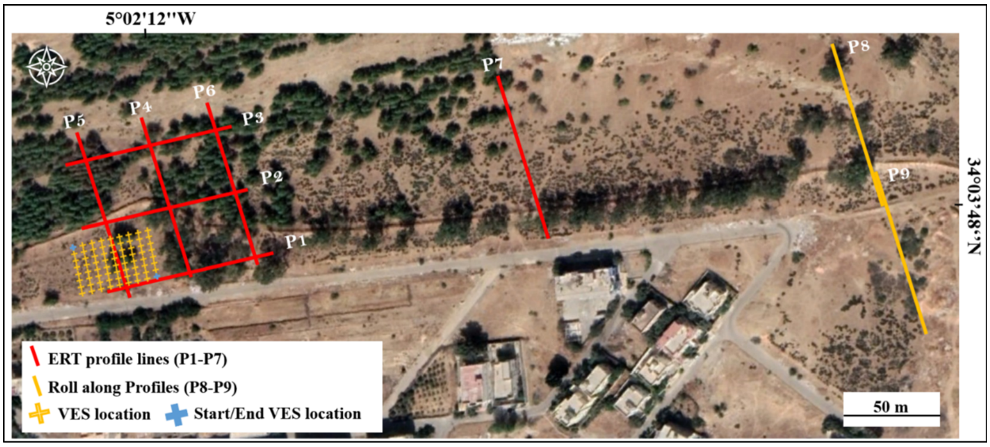

Figure 5. Location of ERT and VES profiles carried out at Tghat-Oued Fez district (Fez, Morocco), (Google Earth 2021).

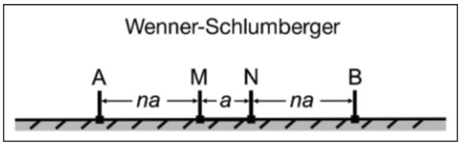

Figure 6. Typical VES electrode arrangement for a Wenner–Schlumberger array (MN = a; AM = $n \times a$). AB: current electrodes. MN: potential electrodes.

maintaining the central position of the electrode array (figure 6). Therefore, as the electrode spacing increases, the depth of investigation increases (Mooney 1980). Measurements were conducted by using a Syscal Pro resistivity meter from IRIS Instruments using a Wenner–Schlumberger configuration (Pazdirek and Blaha 1996) (figure 6). The (AB/2) interval of each VES point was increased from 2 to 80 m to increase the depth of investigation. Given the geometry of the voids in the basement, it is more convenient to use this configuration which is sensitive to both horizontal and vertical structures. The VESs were laid out into a grid constituted by nine equidistant profiles, 5 m apart (figure 5), in which each profile was comprised of 8 VES points oriented following the NNW–SSE direction (figure 5).

Apparent resistivity values were derived using the resolution of the Laplacian electrical potential equation in spherical coordinates, is represented by the following expression (Takahashi and Kawase 1990):

$$\nabla^2 V = \frac{d^2 V}{dr^2} + \frac{2}{r}\frac{dV}{dr} = 0. \tag{1}$$

According to Ohm's law and considering a hemispherical medium, equation (1) could be put under a more appropriate form to provide the apparent resistivity value to Wenner–Schlumberger configuration as follows (Loke 1999):

$$\rho_{\text{app}} = \frac{\Delta V}{I} \times \pi n(n+1)a. \tag{2}$$

Regarding electrical resistivity tomography data acquisition, a Syscal Pro resistivity meter from IRIS Instrument was employed in conjunction with a multicore-based connection system with the capability to simultaneously connect up to 48 electrodes spaced 2 m apart. Thus, the total length of each ERT profile was 96 m. The data acquired are presented in the form of 2D electrical sections of apparent electrical resistivity values, in which the horizontal and vertical axes correspond, respectively, to the x-distance along the profile and the investigation depth reached because of the separation between the two mobile electrodes. In the sections, the measurements are plotted in the middle of the acquisition array at a depth, which is related to the distance of the current electrode separation (Telford *et al.* 1990; Parasnis 1997). Subsoil electrical models showing the cross-sectional distribution of resistivity are derived from the sections using the data inversion method (Loke and Barker 1996; Tarantola 2005; Everett 2013; Kearey *et al.* 2013).

In the present study, the dipole–dipole configuration was used with a total length of 96 m and an electrode spacing of 2 m. The dipole–dipole array (figure 7) is very sensitive to horizontal changes in resistivity, although it is relatively insensitive to vertical changes in resistivity as well (Loke 1999). This means that it is good for the mapping of vertical structures, such as dykes and cavities, but relatively poor for the mapping of horizontally

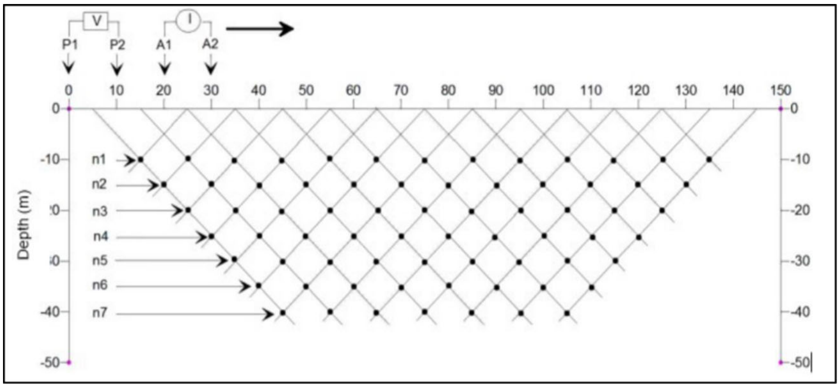

Figure 7. Typical ERT electrode arrangement for a dipole–dipole array. A1, A2: current electrodes. P1, P2: potential electrodes.

layered structures, such as sills or sedimentary basins. The postprocessing and interpretation of the measured data were performed using RES2DINV software from Geotomo Software, which is based on the inversion algorithm described by Loke and Barker (1996).

Electrical resistivity values were collected from nine ERT profiles (figure 5). These ERT profiles, labelled as P1, P2, P3, P4, P5, and P6, respectively, have been arranged in such a way to highlight the contacts between the Glacis/marls/conglomerates layers. P1, P2, and P3 are parallel and oriented ENE–WSW (figure 5). These ERT profiles are separated from each other by half of the total array length (48 m), while the profiles P4, P5, and P6 are perpendicular to them. The whole ERT profile arrangement forms a grid (figure 5), where the goal of which is to be able to make correlations in all directions. Profile P7 is located further east parallel to P4, P5, and P6. Finally, profiles P8 and P9 were laid out on an uninhabited area following a roll-along design at a distance of 100 m apart from P7 (figure 5).

The apparent resistivity values obtained through ERT measurements is derived by the equation provided by Loke (1999):

$$\rho_S = K\frac{\Delta V}{I}. \tag{3}$$

The geometric factor used in ERT measurements with dipole–dipole array is represented by the following expression:

$$K = n(n+1)(n+2)\pi a. \tag{4}$$

Substituting equation (4) into equation (3) and rearranging its terms, we get the apparent resistivity equation, which can be written as follows:

$$\rho_{\mathrm{app}} = n(n+1)(n+2)\pi a\frac{\Delta V}{I}. \tag{5}$$

where ρ_{app} is the apparent resistivity, in Ωm; ΔV is the potential difference, in V; I is the injected current, in A; and a is the distance between current and potential pairs of the electrode, in m. It is worth noting that VES technique, commonly provides apparent electrical resistivity values and ERT technique provides, after inversion process, which is non-unique (Mehanee and Zhdanov 2002; Tarantola 2005), the true resistivity of the subsurface. So the VES technique provides a more qualitative analysis defining the general distribution of resistivity parameters, and the ERT technique a more quantitative interpretation, in terms of electrical properties of the materials in the subsurface (Loke 1999; Karriqi and Alikaj 2011).

3.1 *Numerical modelling and inversion using pyGIMLi and BERT*

Although open-source algorithms for geoelectrical data inversion and modelling have not been widely used in geophysical communities, various open-source algorithms have been developed in recent years (Doyoro *et al.* 2022). The pyGIMLi environment is a structured open-source package with capabilities for electrical geophysical data modelling and inversion (Rücker *et al.* 2017). It is structured because its functionality is reliant on other libraries and a certain version of the Python programming language. All of the methodologies and concepts used in this article are from the free source C++ library GIMLI, which was created as a powerful tool for method-independent inverse problem solutions. The forward operator, which was specifically created for the DC resistivity problem, serves as the application suite's base.

BERT stands for Boundless Electrical Resistivity Tomography.

Günther *et al.* (2006) outline the underlying theory and technology of BERT, which is based on the finite element modelling approaches mentioned by Rucker *et al.* (2006). Initially created for point electrodes, finite element modelling was later expanded to arbitrary electrode forms using the full electrode model (Rücker *et al.* 2017) and lengthy electrodes using the shunt electrode model (Ronczka *et al.* 2015). In general, the inversion is based on smoothness-constrained Gauss–Newton inversion and it was formalized as a flexible minimization and regularization scheme later (Mehanee *et al.* 1998; Tarantola 2005; Mehanee 2022b).

BERT employs a unified data format (UDF) framework that organizes the information included in the geoelectrical datasets entered and guarantees that all information are clearer and more transportable (Günther and Rücker 2022). Specifically, UDF makes it much simpler to comprehend the information included in the program's data and enables completely tailored flexibility in operations such as adding topography, assignments, variable type transformation, copying, and rewriting.

3.2 *1D and 2D ERT modelling and inversion*

We used a direct current (DC) one-dimensional vertical electrical sounding modelling operator to generate data, inversion, and response model for 1D VES inversion for a smooth model. We use the ERTManager in the ERT module of pyGIMLi for 2D ERT inversion (see pygimli.org examples). The Anaconda distribution includes the pyBERT library (anaconda.org/gimli/pybert). We use Jupyter Notebook to import all types of data files that will be processed in JupyterLab, which is a web-based interactive development environment for notebooks, code, and data. Providing users with the ability to configure and arrange workflows in data science, scientific computing, and machine learning (https://jupyter.org/).

ERT measurements provide potential differences from which apparent resistivities can be easily determined. A data inversion is necessary to determine the true resistivities of a heterogeneous subsoil. The data vector is constructed using the logarithms of the measured apparent resistivities. Each data is associated with an error, which is used for weighting in order to determine how close the weighted residual between data (measured apparent resistivity) and model response $f(m)$ (calculated apparent resistivity values), obtained by the forward operator, the data functional ϕ_d or misfit, to be minimized is defined by (Loke and Barker 1996; Mehanee and Zhdanov 1999; Tarantola 2005):

$$\phi_d(m) = \sum_{i=1}^{D} \left| \frac{d_i - f_i(m)}{\varepsilon_i} \right|^2 = \left\| D(d - f(m)) \right\|_2^2 , \tag{6}$$

$$\phi = \phi_d + \lambda \phi_m \rightarrow \min, \tag{7}$$

$$\phi_m(m) = \left\| c\left(m - m^0\right) \right\|_2^2 , \tag{8}$$

ϕ represents the model solution of the Tikhonov regularization for data inversion. ϕ_d is the residual norm. λ is the regularization parameter. ϕ_m is the stabilizer norm, an additional functional model (Tikhonov and Arsenin 1977). D is the diagonal matrix of the inverse of the relative measurement error vector (err). m is the logarithmic apparent resistivity vector log (rhoa), $f(m)$ is the response model of m.

For vertical electrical soundings, numpy numerics, mpl plotting, pygimli, and the 1D plotting function are all imported using this algorithm, as a command for importing 1D geoelectric data output formats (.bin or .csv) which could be transformed into the unified data format. All the VES were processed using the algorithms below:

```
import numpy as np
import matplotlib.pyplot as plt
import pygimli as pg
from pygimli.viewer.mpl import drawModel1D
import pygimli as pg
from pygimli.physics import VESManager
# Source: Authors and pyGIMLi.
ax, _ = ves.showModel(model)
ves.fop.drawModel(ax, synthModel)
ab2, mn, ra = np.genfromtxt("filename", unpack=True)
err = np.ones_like(ra) * 0.03
ves = VESManager(ab2=ab2, mn2=mn/2)
model = ves.invert(ra, err, nLayer=4,
    showProgress=0, verbose=1)
ves.showModel(model)
ves.showFit()
```

All the ERT profiles were processed with finite-element modelling inversion using the algorithms below:

```
import numpy as np
import pygimli as pg
from pygimli.physics import ert
import pybert as pb
from pygimli.physics import ert
import pybert as pb
# Source: Authors and pyGIMLi.
data = pb.load('filename')
print(data)
data['k'] = ert.createGeometricFactors(data)
data['rhoa'] = data['u'] / data['i'] * data['k']
data['err'] = ert.estimateError(data)
ert.show(data)
x, z = np.genfromtxt("topographyfile", encoding="UTF",
skip_header=3, unpack=1, usecols=(0, 1),
    delimiter="\t")
print(len(x))
for i in range(data.sensorCount()):
data.setSensor(i, [x[i], 0, z[i]])
data.save("data.dat")
manager = pg.physics.ert.ERTManager(data, sr=True,
    verbose =True)
inversion = manager.invert(lam=5, paraMaxCellSize=1,
paraBoundary=0, paraDepth=20 Zwight=0.4)
manager.showResult(cMin=3, cMax=110, xlabel="x (m)",
    ylabel="z (m)");
plt.savefig("fileformat",dpi=1200, bbox_inches="tight")
```

4. Results and discussion

4.1 *Apparent resistivity maps*

The VES isoresistivity contour map for AB/2 = 10 m shown in figure 8 represents the lateral variation of apparent resistivity values in a horizontal plane at a depth of approximately 2.5 m. The presence of a homogeneous layer associated with the conductive marl deposit, which dominates the subsurface is identified. The southern part of the map shows relatively higher resistivity values compared to the rest of the area, ranging between 12 and 16 Ωm. This more resistive region can probably be associated with a glacis-marl passage, which can be explained by soil compaction given the softening of the slope and the proximity to the road.

Figure 8(b and c) shows the apparent isoresistivity contour maps for AB/2 = 30 m and AB/2 = 40 m, at a depth of approximately 7–10 m. These two maps reveal a very regular distribution of low resistivities in the southern part. This low-resistivity region highlights the influence on these electrical values of the presence of a more homogeneous marly horizon. In this case, it emphasizes the predominance of the most abundant marly formation which contains mostly gypsum concretions. At this depth, the rock is soft, which means it is more vulnerable to alteration. Also, water infiltration accelerates gypsum dissolution, leading to crack formation, which grows with time to create voids and cavities in the subsurface.

Figure 9(a) illustrates the apparent resistivity distribution contouring in a horizontal plane for AB/2 = 50 m. This map identifies low resistivity values located in the southern part attributed to marly material characterized by apparent electrical resistivity values below 9 Ωm. Marl-bearing formations are characterized by a relevant thickness of 15 m on average, which explains its significant influence on those more conductive values on the contour map (figure 9a). On the other hand, on the upper part of the isoresistivity map, relatively high resistivity values are displayed compared to the remaining areas of the same map. By comparing this apparent resistivity contour map with the previous ones, it can be stated that as depth increases, the apparent resistivity values assigned to deeper formations also increase, especially in the central part. Furthermore, the marly formation, at deeper horizons, also presents higher resistivity values, contrary to the common tendency for this marl-bearing material (figures 8c and 9a). This is likely attributed to the presence of cracking and alteration phenomena.

Based on the results of the isoresistivity contour map for AB/2 = 60 m shown in figure 9(b), the expansion of a more resistive structure can be observed within the conductive marl-bearing horizon. This elongated structure, located between longitude values –5.03685 and –5.0368, was already evident in the previous isoresistivity map starting at a 10 m depth. This electrical discontinuity infers a potential cavity of significant size, which progresses in depth as well. The latter is supported by the significant presence of abundant cracks and fissures outcropping on the surface. Then, this resistive zone can be

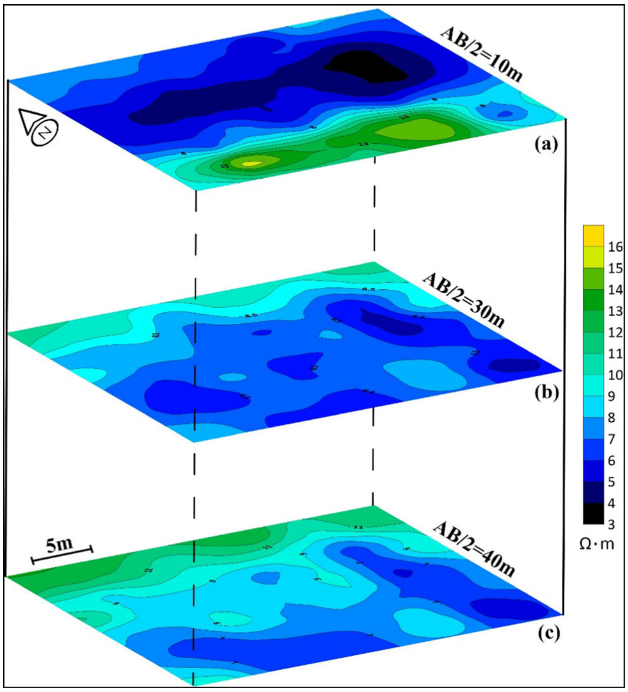

Figure 8. Iso-apparent resistivity contour maps for **(a)** AB/2 = 10 m, **(b)** AB/2 = 30 m, and **(c)** AB/2 = 40 m.

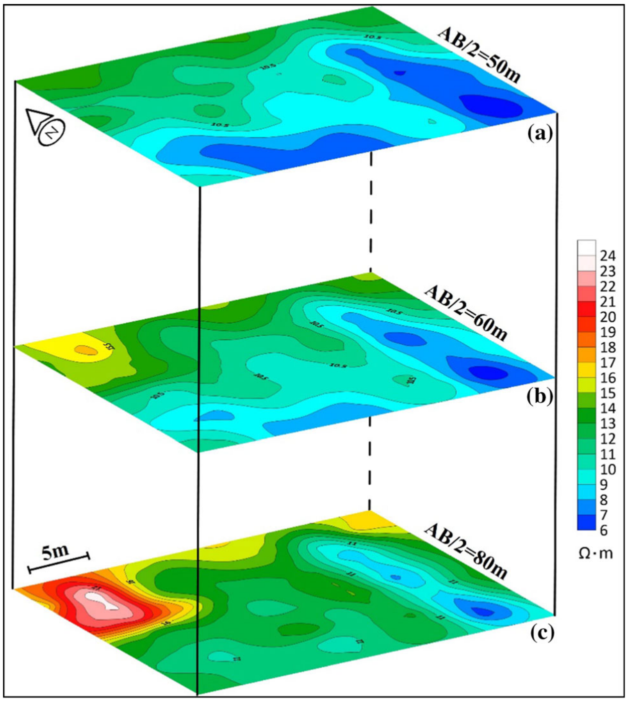

Figure 9. Iso-apparent resistivity contour maps for **(a)** AB/2 = 50 m, **(b)** AB/2 = 60 m, and **(c)** AB/2 = 80 m.

pinpointed as a cavity filled with loose sediments and considered as the main reason for the surficial subsidence observed in the central part of this area.

The last isoresistivity contour map (figure 9c) represents the maximum AB spacing for this study, which corresponds to a horizon of 20 m depth. Compared to the previous two maps, it illustrates the same tendency of resistive values attributed to the presence of a cavity in this region as a result of marl-bearing formations dissolution phenomena. This electrical anomaly reflects an elongated north–south direction structure extending towards the middle of the contour map. On the other hand, at the upper-left side, the contour map emphasizes the highest apparent resistivity values indicating the beginning of a more stiffed conglomeratic formation. This resistive anomaly highlights the presence of massive deposits of conglomerate. These compact formations are present in the region following verticalized structures due to past compressional tectonic efforts by the South-Rifin Fault, which is oriented to the south in Tghat Mountain (Charroud *et al.* 2006; Cherai *et al.* 2008). The presence of this hard layer at this depth, especially in the northern part, is confirmed by geological inspections as well as inferred by ERT profiles, which are examined in the next section.

4.2 *1D inversion of VES data*

IPI2win software and Python-based codes, by means of pyGIMLi library implementation, were used to process and invert 1D VES data. Both tools have the capability to generate a resistivity model that best fits the observed and calculated resistivities. IPI2win software uses linear filtering for the forward calculation of geological models and a regularized optimization based on Tikhonov's approach for the inverse solution (curve fitting), and the algorithm uses smoothness-constrained inversion for curve fitting that aims to find the model that best fits the data while also being smooth (having a smooth curve or surface). This is often done by adding a smoothness constraint to the optimization problem that is being solved.

We have chosen two electrical soundings located more exactly in the area which show higher resistivity values which are attributed to the presence of cavities in the study area, the two soundings are in the same line of altitude spaced 5 m further north. These soundings consist of 6 spacings AB and MN to reach an average depth of 20 m, the curves on (figure 10a, b are processed using IPI2win which is an automatic and manual 1D interpretation program for VES curves, while the two soundings that follow (figure 10c, d) were processed using the algorithm already described employing

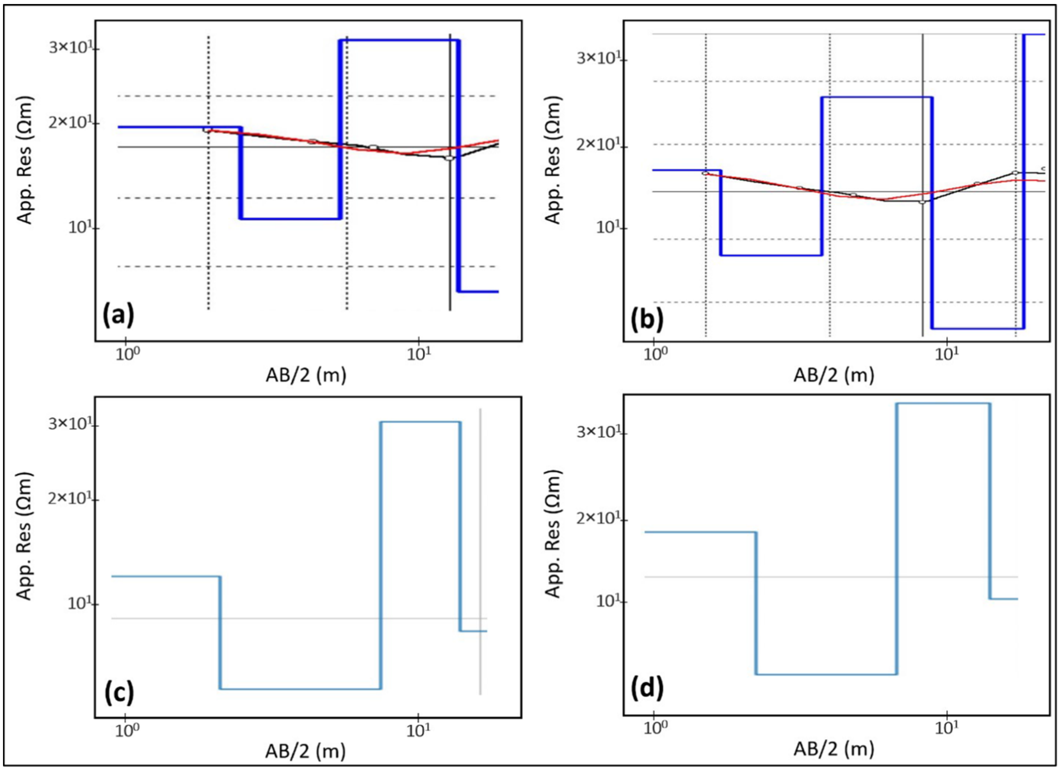

Figure 10. Quantitative interpretation of vertical electrical sounding **(a, b)** processed by IPI2win and **(c, d)** processed by pyGIMLi.

the pyGIMLi platform. The objective of having an order of magnitude of the resistivities corresponding to the different layers of ground recognized and therefore to help in the interpretation of the variations of resistivity in the geophysical survey. The analysis of the four electrical-sounding curves shows that, overall, there is a resemblance between them. The number of layers highlighted is the same for the two first and last soundings.

In order to attribute to each layer, the corresponding geological formation, we relied on the range of electrical resistivity corresponding to each geological formation that we could measure independently for each of these formations. The correlation between these values, the geology of the region, and the average geoelectrical resistivity of these formations made it possible to highlight four formations for the VES1 and VES2 surveys.

The interpretation of the measurements of VES1 and VES2 curves indicates five successive resistivity ranges:

- 0–2.5 m: Glacis coverage with average resistivity values from 13 to 14 Ωm in both curves.
- 2.5–5 m: Marly material characterized by apparent electrical resistivity values lower than 4 Ωm in both curves.
- 5–10 m: Higher resistivity layer, linked to the presence of a cavity filled with solid sediment within the marl, it is the same observation on the isoresistivity map (figure 9b) within the conductive marly layer, the resistivity value of this formation varies between 40 and 42 Ωm.
- 10–21 m: A second conductive layer of marl with a lower resistivity value lower than 4 Ωm.
- from 21 m: Very high resistivity value attributed to the appearance of the conglomeratic roof, a resistant formation showing values that can go up to more than 1000 Ωm, if they are compact and solidified.

The quantitative interpretation of this survey provides information on the electrical distribution of the study area up to almost 20 m deep. The two curves processed by pyGIMLi are more identical to the month with the first two curves, the RMS values are set at 3%. The proposed models (figure 9) globally show four ranges of resistivities. They oscillate between 1 and 40 Ωm. They decrease from the surface where resistivities of the order of 14 Ωm are recorded down to a depth of 3 m where they rise to more than 4 m. This increase is mainly related to the presence of the cavity filled with more consolidated sediment included in the marly matrix which constitutes the most extensive basement of the site. Rainwater promotes the dissolution of gypsum concretion within the marl and causes the filling of these empty cavities by solid slope materials, hence the appearance of these resistive anomalies.

4.3 *ERT and BERT modelling results*

The two algorithms used in this article are marginally different inversion parameters for processing the data, therefore only allowing qualitative comparison. The datasets were processed by RES2DINV with a non-linear optimization technique for determining 2D resistivity distribution (Griffiths and Barker 1993). The least-squares equation for the inversion was solved using the standard Gauss–Newton optimization technique to reduce the apparent resistivity differences between the measured and calculated pseudo-sections (Loke and Barker 1996). The iterations continued until the data converged and the appropriate damping factors for the inversion were selected based on the estimated noise level on the measured data to reduce iteration count, by estimating the best damping factor that provides the least root mean square error. The damping factors for the datasets ranged from 0.02 to 0.15. The BERT inversion is based on a smoothness-constrained Gauss–Newton inversion described by Gunther *et al.* (2006). Additionally, the inversion specifies several measures of data fit in order to fit the data better, the regularization parameter is decreased using LAMBDA=5, and the inversion algorithm was allowed to continue until the RMS convergence limit of 3% was reached. The inversion output parameters, including the number of iterations, RMS error, and the initial and the final chi-square fit are listed in table 1.

The ERT profiles acquired in the study area aimed to characterize the near-surface geology and to help infer the presence of potential landslide form, cavities, and voids and as a result explain the presence of the evidence on surface of the occurrence of cracking and soil subsidence phenomena.

In that way, the showed 2D electrical sections from ERT P1 profile (figure 11a), which was obtained with a very acceptable root mean square error (RMSE) of 2.6%, reveal two distinctive ranges of electrical resistivity values featuring two different resistive regions. The first region consists of a resistive layer, showing resistivities <30 Ωm with a thickness ranging from a few decimeters to less than 3 m, is referred to as the glacis colluvial cover. Conversely, the second region is constituted by a more conductive and predominant horizon with resistivities ranging from 5 to 12 Ωm (figure 11a). This conductive layer is associated with late Pliocene green marl-bearing material, which is dominant in this electrical section. Additionally, a very delimited round-shaped resistive anomaly appears at the upper-left side of the electrical section (figure 11a), which is assumed to be a near-surface cavity explaining the presence of significant cracks outcropping on surface.

Table 1. *2D inversion utilizing BERT, showing the number of iterations, chi-square, and RMS error displayed.*

	Inversion iteration	chi^2 (initial and final)	RMS (%)
BERT P4	4	10.15/0.6	3.02
BERT P5	6	50.96/1.35	3.03
BERT P6	6	36.11/0.63	3.02
BERT P7	5	24.05/0.5	3.02
BERT P8	4	12.17/0.76	3.01
BERT P9	3	14.52/0.47	3

The ERT P2 electrical section (figure 11b) emphasizes three distinct resistive areas associated to different geologic formations. Thus, it is distinguishable that a more widespread surficial and resistive layer associated to the colluvial cover unit characterized by high resistivity values, approximately above 30 Ωm, and reaching a maximum depth of 4 m. Then, a second conductive layer is illustrated, which is associated to the marly horizon, whose thickness is variable ranging roughly from 6 m, in the middle, to 12 m, in the westmost part (figure 11b). This conductive layer spotlights two relatively resistive round-shaped zones, which are interpreted as two near-surface cavities or areas subject to dissolution processes. The third electrical layer corresponds to the conglomeratic formation presents at 10 m depth and is characterized by the highest electrical values ranging from 30 to 100 Ωm.

The 2D electrical section, from ERT P3 profile, was generated with an RMSE of 1.9%, defining the inversion process as valid (figure 11c). This electrical section shows two predominant and resistive layers: surficial glacis deposits covering the surface up to 4 m depth, and conglomerates appearing on the right side of the electrical section from a depth of 5 m. Also, it is distinguishable on the electrical section (figure 11c) a more conductive layer attributed to the marl-bearing formation,

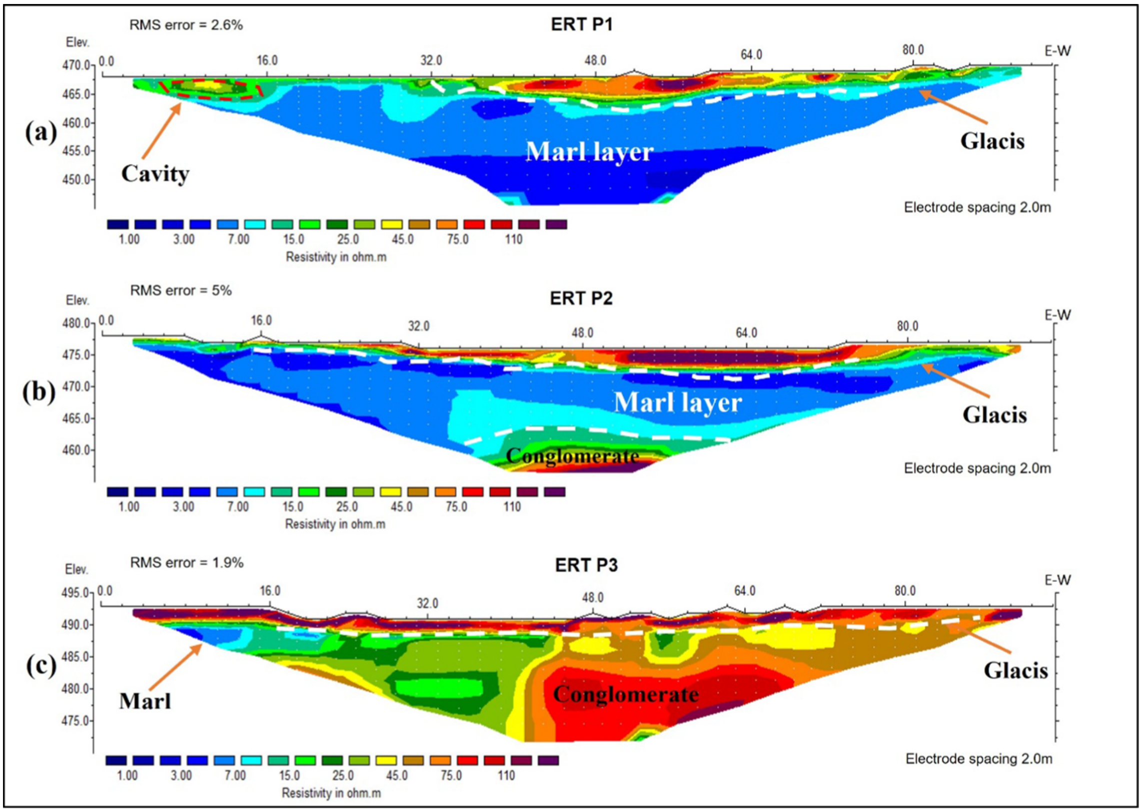

Figure 11. 2D electrical sections from: **(a)** ERT P1, **(b)** ERT P2, and **(c)** ERT P3.

indicating a decrease in the thickness of this formation to the north.

Figure 12 depicts electrical sections from ERT P4 and P5 profiles, respectively, laid out perpendicularly to the previous ones, following the NNW–SSE direction (figure 5). The ERT P4 electrical section (figure 12a) shows an extended and surficial resistive layer that, as it was mentioned above, represents glacis deposits. In contrast, from 4 m depth appears a conductive layer characterized by electrical resistivity values between 2 and 10 **Ω**m. This conductive layer would correspond to green marl deposits. On the other hand, following the same tendency as discussed previously, a highly resistive layer is attributed to hard conglomerates formation. This more resistive layer thickness varies along the electrical section depending on its geometry, also revealing a dipping-shaped structure oriented towards the south, marked on the electrical section (figure 12a).

ERT P5 profile was carried out overlapping VES positions. The ERT P5 electrical section illustrates a similar distribution of resistivity values to those examined from the previous profile. In fact, this electrical section similarly shows the same extended surficial resistive layer associated with glacis deposits. Also, a second conductive layer, showing resistivity values ranging from 2 to 8 **Ω**m, is distinguishable in the section and attributed to Late Pliocene marls formation. Unlike the previous electrical section, this electrical section presents an elongated resistive anomaly embedded in the conductive layer, which is interpreted as a possible near-surface cavity filled with loose sediments because of dissolution processes. Indeed, the position of this anomaly coincides perfectly with the position of a similar elongated structure obtained in the isoresistivity contour maps for an AB/2 spacing between 60 and 80 m (figure 9). Moreover, ERT P5 electrical section might infer a fault (marked on the section), which would explain the verticalization of Pliocene conglomerates and the deformation of Quaternary glacis deposits of the study area. This interpretation agrees with in-field geologic observation as well as previous works by Charroud *et al.* (2006) on the southern slope of Tghat, whose work demonstrated a more recent tectonic activity.

The ERT P6 electrical section was obtained with an RMSE of 3%, meaning that the inversion-based

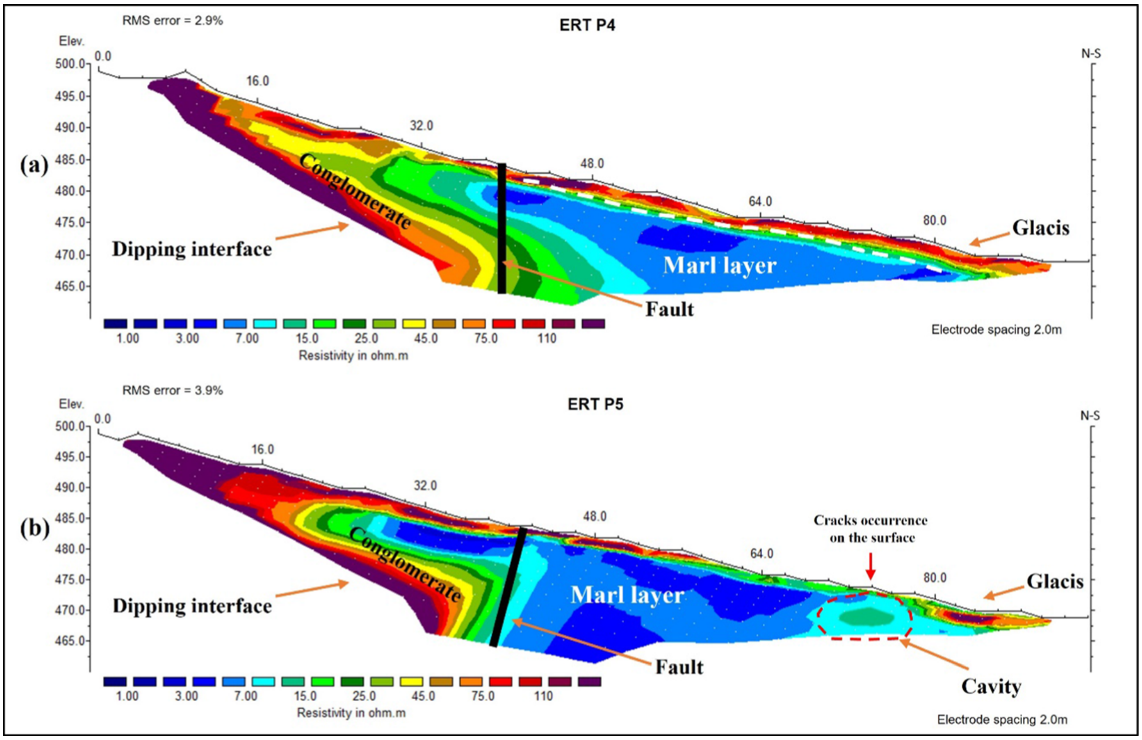

Figure 12. 2D electrical sections from: **(a)** ERT P4 and **(b)** ERT P5.

process fitting was appropriate (figure 13a). Similarly, this electrical section shows the three electrical layers attributed to the three main formations of the study area in terms of actual resistivity values. A first electrical layer corresponding to a surficial and widespread zone of high resistivity values extended downward till 4 m depth and attributed to the glacis unit. Then, a low resistivity layer is associated with the marl bearing formation, whose thickness increases to the south. This conductive layer reveals the presence of a relatively high resistivity anomaly, like the previous one observed in ERT P5 (figure 12b). Similarly, this embedded anomaly might infer the presence of a near-surface cavity filled with loose sediments. Moreover, the conglomerate deposits influence the electrical values, giving rise to the same observed dipping-shaped structure forward to the south, similarly observed in ERT P5 and P6 sections. Thus, this consistency in the type of anomaly pattern supports the suggestion of a particular south-oriented tectonic compressional regime exerted by the South-Rifin Fault.

The ERT P7 electrical section was generated after inversion processing with an RMSE of 6.9%, somehow validating the suitability of the data. This ERT profile was laid out to identify lateral variations due to the presence of near-surface voids within the marly formation at positions located further from ERT P4, P5 and P6 profile set-up (figure 5). As mentioned, this electrical section follows the same pattern in terms of electrical layers, in which the presence of the marl formation contributed to producing the most conductive layer, whose electrical resistivity values are roughly below 20 Ωm. This conductive layer does not show evidence of any void occurrence in terms of electrical resistivity anomalies, which is consistent with the absence of cracks or subsidence phenomena on the surface in this part of the study area. Also, the most surficial resistivity layer, which is laid out along the whole electrical section with a thickness of about 3–4 m, is associated with the glacis cover deposits. Similarly, the most resistive layer is associated to the hard conglomerate formation, characterized by electrical resistivity values above 50 Ωm. The thickness of this electrical layer is variable depending on the geologic geometry, which shows a sinking structure towards the south, keeping the consistency of this aforementioned tendency.

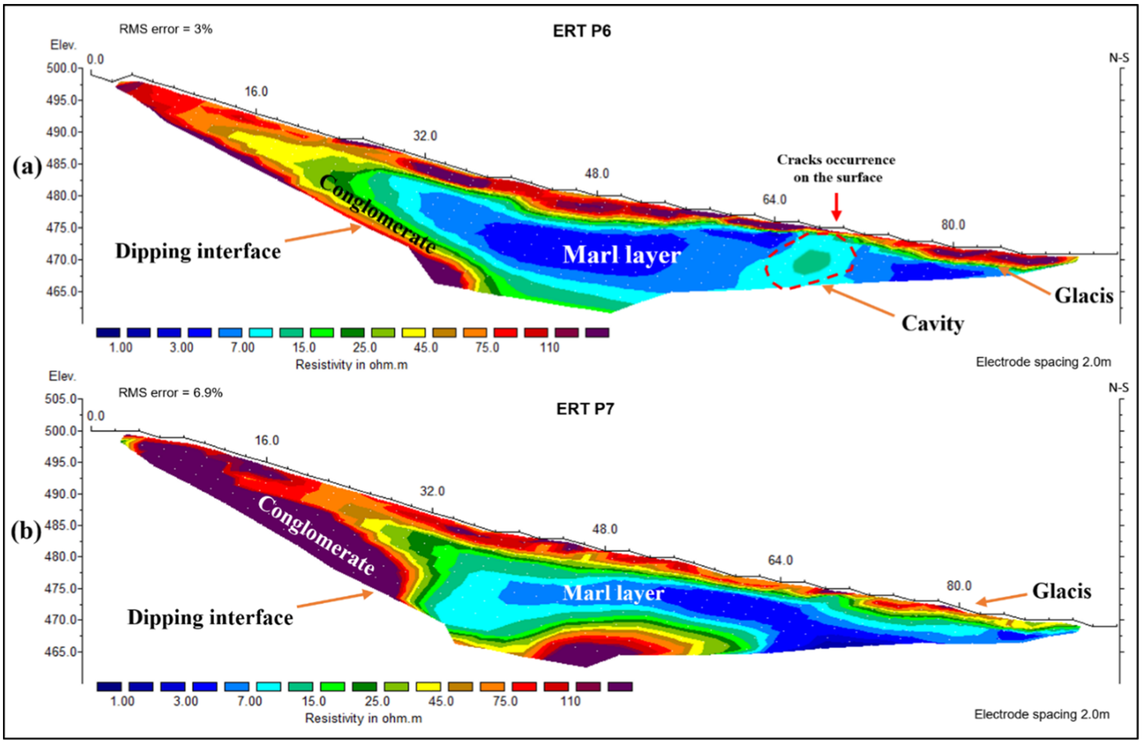

Figure 13. 2D electrical sections from: **(a)** ERT P6 and **(b)** ERT P7.

ERT P8 and P9 profiles constitute a combined ERT profile, named ERT P8 and P9 roll-along profile, in which the ERT P9 profile is an extension of the ERT P8 profile (figure 5). These profiles were set up based on the geological inspections of the study area and the findings from previous research (Charroud *et al.* 2006). These findings indicated that the conglomerate horizon takes a more horizontal position downstream of Tghat Mountain and geologic inspections suggested the presence of a bulging between the upstream and downstream of the mountain. Figure 14(a) depicts the ERT P8 electrical section obtained with an RMSE of 3%, giving validity to the processed data. The presence of the three typical electrical levels for the study area already mentioned is associated with distinct geological formations described above. ERT P8 electrical section also reveals a dipping electrical interface inferring the dipping conglomerate formation at this point, already observed on those previous ERT profiles coincidently with the same orientation.

On the other hand, the ERT P9 electrical section, obtained with an RMSE of 2.2%, shows a horizontally layered arrangement of the main three electrical layers. The surficial resistive layer associated with glacis cover deposits presents greater thickness than that observed on the northern electrical sections (up to 5 m) (figure 14b). The latter is explained by the location of this profile, which was situated downstream to the south (figure 5), and the accumulation of more sediment transported and settled by runoff and erosion phenomena. Furthermore, it can be observed the starting of a horizontal high resistive level at a depth of 18 m, which is attributed to the conglomerate formation presence.

For BERT modelling results, we chose to process inversion only for profiles that display the appearance of a landslide shape, namely from BERT4 to BERT9. All the resulting tomograms are shown in figure 15 with the once inverted with RES2DINV, for a more comparative presentation. The inversion is performed using the invert function of the ERTManager class, which includes several optional parameters to control the behaviour of the inversion. In this case, the inversion is being performed with a regularization parameter of LAMBDA=5, a maximum cell size of 1, a boundary parameter of 0, a depth parameter of 30, and a weight parameter of 0.4. The BERT profiles have a chi-squared misfit close to one, and the same reduced regularization value for all profiles to

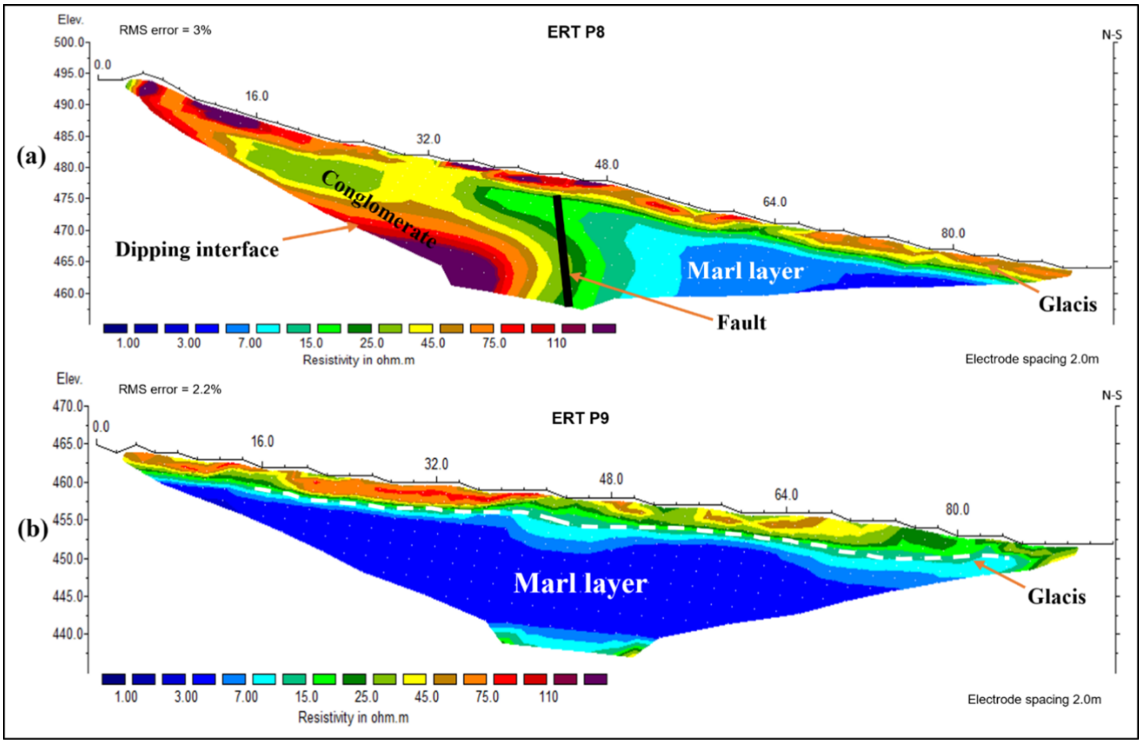

Figure 14. 2D electrical sections from: **(a)** ERT P8 and **(b)** ERT P9.

improve data fit, resulting in a relative rms error of about 3% for all profiles (table 1).

The form of landslides can be observed on the following profiles: BERT4 (figure 15) which has a superficial resistive horizon throughout the profile with a resistivity range greater than 100 Ωm and a second more resistant horizon with a resistivity range greater than 150 Ωm, which is correlated with the hard conglomerates showing a type of sliding form to the south. The landslide is approximately 5–25 m deep. This profile highlights the lack of a true transition plane between glacis and conglomerates. Finally, the marly formation is a homogeneous and conductive layer that occupies the entire zone to the south and has resistivity values less than 10 Ωm.

The BERT5 profile has three distinct horizons (figure 15): The first resistive zone with values greater than 100 Ωm, formed by cover glacis, is wider in the north and thins in the south (less than 1 m deep). The second zone is located in the central and southern part of the profile, shown in blue colour on the profile, these are homogeneous and conductive marls displaying resistivity values less than 10 Ωm. Further south a resistive anomaly close to the surface is very clear on the profile, this anomaly is attributed to a cavity resulting from gypsum dissolution and filling by materials of the slope more solid than the conductive encasing marly layer, the same anomaly was highlighted in the ERT P5 (figure 12). The third formation is the conglomerate deposits, which are found further north and are a denser and more resistive horizon with values greater than 150 Ωm exhibiting the same type of sliding towards the south.

The profiles BERT6 and BERT7 (figure 15): have nearly the same distribution of the three formations already described in the study area, starting with a resistive layer along the length of the two profiles, followed by a marly conductor and homogenous layer displaying resistivity less than 10 Ωm, and finally, the most resistive layer (greater than 150 Ωm) attributed to the hard and dense conglomerates showing the sliding form toward the south.

For the BERT8 profile (figure 15): we notice the presence of the same lithological arrangement described in the previous profiles, but we also notice the presence of tiny conductive zones and of enlarged shape on the upper left side, between the two resistive formations of superficial glacis and the conglomerate layer, which could be explained

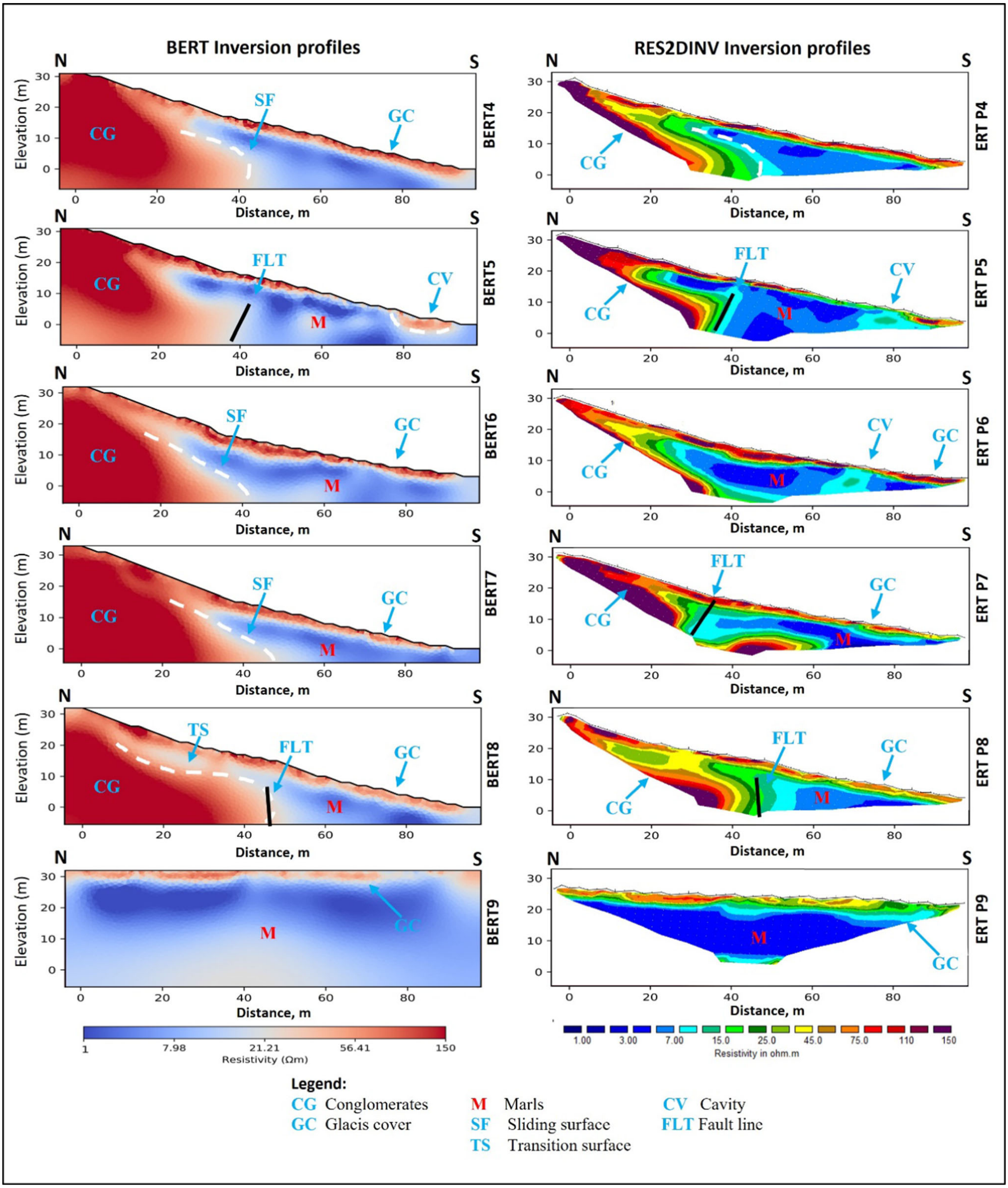

Figure 15. 2D electrical sections from: BERT Inversion (left) including BERT4, BERT5, BERT6, BERT7, BERT8, BERT9, and RES2DINV Inversion (right) ERT P4, ERT P5, ERT P6, ERT P7, ERT P8, ERT P9.

by the presence of internal water content. These conductive zones could be associated with the most active part of the sliding mechanism. Moreover, the presence of water has a significant influence on the triggering of the landslide process and, as a result, the creation of slope instability.

The BERT9 profile (figure 15): on the other hand, shows the three main electrical layers arranged in horizontal layers, similar to the ERT P9. This profile demonstrates a strong electrical contrast between the high resistivity values of the cover material and those of the conductive marls below. The superficial glacis layer, which has resistivity values around 100 Ωm is thicker than the other profiles (up to 5 m deep), this layer is followed by a second marly level that is homogeneous and conductive. Then, at a depth of 18 m, there is a more or less stable ground with increasing resistivities in depth, which is attributed to the appearance of the conglomeratic roof.

5. Conclusion

This work was carried out to describe the subsurface structure and the detection of possible near-surface voids and cavities in the Tghat-Oued Fez area, Morocco, by means of two electrical-based geophysical techniques: electrical resistivity tomography (ERT) technique and vertical electrical sounding (VES) technique. VES-based surveying enabled qualitatively distinguishing different subsurface rock units based on their apparent resistivity property contrasts. Thus, higher resistivity values were observed along the northern parts of the isoresistivity contour maps associated to the hard conglomerate formations. Conversely, lower resistivity values were identified in the southern part of the study area attributed to marl-bearing formations. In the study area, the potential void occurrence has been associated with marl-bearing formation because of dissolution processes. VES surveying highlighted near-surface resistive anomalies embedded into the marl-bearing conductive layer attributed to these void occurrences supported by some evidence of cracks and subsidence phenomena observed on the surface.

On the other hand, the two free inversion software packages tested were capable of resolving the fundamental issues. pyGIMLi and BERT could also be useful for inverting and modelling geoelectrical data, producing results comparable to well-known processing software. The electrical resistivity tomography technique enabled the qualitatively identifying the different geological formations in terms of actual resistivity values associated with those formations. The predominant formations inferred from ERT surveying in the study area were surficial glacis cover deposits, characterized by moderate resistivity values, marls bearing formations, defined by more conductive values, and hard conglomerate formations associated with the most resistive values. Also, ERT enabled to infer the geometry of those geological formations, and interface positioning such as a lateral variation of materials, faulting, etc. The placing of different inferred formations by ERT coincides with that one derived from the VES technique. In line with the VES findings, the ERT survey enabled us to identify, as well, some resistive anomalies, attributed to void occurrences, into the more conductive layer associated to marls-bearing formation. Again, these void occurrences are supported by surficial cracks and subsidence phenomena outcropping on the surface.

It is worth noting that this research is still in progress and, as part of additional study stages, before further urban development, is planned to undertake boreholes campaigns, along with a seismic refraction tomography and ground penetrating radar survey, whose timing would depend on final budgetary decisions. These planned boreholes and surveys would be addressed on the inferred sliding form and void positions enabling a more precise knowledge of the internal geologic structure of the area under urban development planning.

Overall, it can be stated that electrical-based geophysical methods are promising non-invasive tools because of the wide coverage, quick data acquisition, and effective cost, which support other complementary and more invasive techniques. These techniques could be used successfully to delineate and map subsurface cavities and landslide areas that might have an important impact on essential infrastructures, or buildings planned to be undertaken in those void-prone areas.

Acknowledgements

We would like to take this opportunity to acknowledge the time and effort devoted by two anonymous reviewers for their critical comments that significantly improved the manuscript.

Author statement

Conceptualization, methodology, software: Oussama Jabrane, Driss El Azzab, Mohammed Charroud. Inversion software and validation: Pedro Martínez-Pagán and Marcos A Martínez-Segura.

Investigation and resources: Oussama Jabrane, Driss El Azzab, Mohammed Charroud, Bouabid El Mansouri, Mahjoub Himi, and Mohammed Elgettafi. Data curation and writing-original draft preparation: Oussama Jabrane. Writing, reviewing and editing: Oussama Jabrane, Pedro Martínez-Pagán and Driss El Azzab. Supervision and project management: Driss El Azzab and Pedro Martínez-Pagán.

References

Ahmamou M, Conrad G and Plaziat J 1989 Réinterprétation des conditions de dépôt des calcaires fluviatiles, lacustres et palustres du bassin ploi-quaternaire ancien sur la bordure nord du bassin du Saiss (Maroc); *Méditerranée* **2(3)** 41–49.

Anaconda.org, Boundless Electrical Resistivity Tomography [online] 2022, https://anaconda.org/gimli/pybert.

Arjwech R, Ruansorn T, Schulmeister M, Everett M E, Thitimakorn T, Pondthai P and Somchat K 2021 Protection of electricity transmission infrastructure from sinkhole hazard based on electrical resistivity tomography; *Eng. Geol.* **293** 106318, https://doi.org/10.1016/j.enggeo.2021.106318.

Balkaya Ç, Göktürkler G, Erhan Z and Ekinci Y L 2012 Exploration for a cave by magnetic and electrical resistivity surveys: Ayvacık Sinkhole example, Bozdağ, İzmir (Western Turkey); *Geophysics* **77** B135–B146.

Bargach K, Ruano P, Chabli A, Galindo-Zaldivar J, Chalouan A, Jabaloy A, Akil M, Ahmamou M, Sanz De Galdeano C and Benmakhlouf M 2004 Recent Tectonic Deformations and Stresses in the Frontal Part of the Rif Cordillera and the Saïss Basin (Fez and Rabat Regions, Morocco); *Pure Appl. Geophys.* **161** 521–540.

Boualla O, Fadili A, Najib S, Khalid M, Makan A and Zourarah B 2021 Assessment of collapse dolines occurrence using electrical resistivity tomography: Case study of Moul El Bergui area, Western Morocco; *J. Appl. Geophys.* **191** 104366, https://doi.org/10.1016/j.jappgeo.2021.104366.

Caleb L and Anthony J W 2022 Underground cavity detection through group dispersion of a GPR signal; *Remote Sens.* **14** 4808.

Carbonel D, Rodríguez-Tribaldos V, Gutiérrez F, Galve J P, Guerrero J, Zarroca M, Roqué C, Linares R, McCalpin J P and Acosta E 2015 Investigating a damaging buried sinkhole cluster in an urban area (Zaragoza city, NE Spain) integrating multiple techniques: Geomorphological surveys, DInSAR, DEMs, GPR, ERT, and trenching; *Geomorphology* **229** 3–16.

Cardarelli E, Cercato M, Cerreto A and Di Filippo G 2010 Electrical resistivity and seismic refraction tomography to detect buried cavities; *Geophys. Prospect.* **58** 685–695.

Charroud M, Cherai B, Benabdelhadi M, Charroud A, El Moutaouakkil N, Falguères C and Lahrach A 2006 Sedimentary evolution of a fore-chain Sais basin during plio-quaternary and modalities of tectonic inversion (Sais basin, Morocco); *Geophys. Res. Abst. Eur. Geosci. Union* **8** 10039.

Charroud M, Cherai B, Benabdelhadi M and Falgueres C 2007 Impact de la néotectonique quaternaire sur la dynamique sédimentaire du Saïs (Maroc): Du bassin d'avant fosse pliocène au plateau continental quaternaire; *Quaternaire* **18(4)** 327–334.

Cherai B, Charroud M, Lahrach A and El Moutaouakil N 2004 Le front sud rifain une expression complexe d'une tectonique tangentielle à la limite du bassin de Sais au Mio-Pliocène et au Quaternaire (Région de Fès, Maroc); *Colloque international à la mémoire de Feue A. Faure Muret*, Rabat, Maroc, 13.

Cherai B, Charroud M, Julien B, Gourari L and Benabdelhadi M 2007 Impact de la néotectonique et des mouvements verticaux sur le réseau hydrographique du Sebou au Quaternaire; *La 4ème Rencontre des Quaternaristes Marocains* (RQM4), Du 15 au 17 Novembre 2007, Oujda, Maroc, 36p.

Cherai B, Charroud M, Lahrach A and Babault J 2008 Influence de la tectonique compressive et des mouvements verticaux d'origine mantellique sur l'évolution quaternaire du Saïs entre le Rif et le Moyen Atlas ; *Actes RQM4*, Oujda, pp. 171–181.

Cook J C 1965 Seismic mapping of underground cavities using reflection amplitudes; *Geophysics* **30(4)** 527–538.

Doyoro Y G, Chang P Y, Puntu J M, Lin D J, Van Huu T, Rahmalia D A and Shie M S 2022 A review of open software resources in python for electrical resistivity modelling; *Geosci. Lett.* **9(1)** 3, https://doi.org/10.1186/s40562-022-00214-1.

Essa K S, Mehanee S, Soliman K and Diab Z E 2020 Gravity profile interpretation using the R-parameter imaging technique with application to ore exploration; *Ore Geol. Rev.* **126** 103695.

Essa K, Mehanee S and Elhussein M 2021 Magnetic data profiles interpretation for mineralized buried structures identification applying the variance analysis method; *Pure Appl. Geophys.* **178** 973–993, https://doi.org/10.1007/s00024-020-02553-6.

Everett M E 2013 Near-Surface Applied Geophysics; Cambridge University Press, https://doi.org/10.1017/CBO9781139088435.

Faugères J C 1978 Southern Rifan Ridges. Sedimentological and Structural Evolution of an Atlantico–Mesogean Basin of African Margin; Thesis, University of Bordeaux I, Talence, 480p.

Fu Z, Ren Z, Hua X, Shi Y, Chen H, Chen C, Li Y and Tang J 2020 Identification of underground water-bearing caves in noisy urban environments (Wuhan, China) using 3D electrical resistivity tomography techniques; *J. Appl. Geophys.* **174** 103966, https://doi.org/10.1016/j.jappgeo.2020.103966.

Gambetta M, Armadillo E, Carmisciano C, Stefanelli P, Cocchi L and Tontini F C 2011 Determining geophysical properties of a near-surface cave through integrated microgravity vertical gradient and electrical resistivity tomography measurements; *J. Cave Karst Stud.* **73** 11–15.

Gan J, Li H, He Z, Gan Y, Mu J, Liu H and Wang L 2022 Application and significance of geological, geochemical, and geophysical methods in the Nanpo Gold Field in Laos; *Minerals* **12** 96, https://doi.org/10.3390/min12010096.

Gibson P J, Lyle P and George D M 2004 Application of resistivity and magnetometry geophysical techniques for near-surface investigations in karstic terranes in Ireland; *J. Cave Karst Stud.* **66(2)** 35–38.

Göktürkler G, Balkaya C and Erhan Z 2008 Geophysical investigation of a landslides: The Altindag landslide site, Izmir (western Turkey); *J. Appl. Geophys.* **65(2)** 84–96, https://doi.org/10.1016/j.jappgeo.2008.05.008.

Gómez-Ortiz D and Martín-Crespo T 2012 Assessing the risk of subsidence of a sinkhole collapse using ground penetrating radar and electrical resistivity tomography; *Eng. Geol.* **149–150** 1–12, https://doi.org/10.1016/j.enggeo.2012.07.022.

Grandjean G 2006 Imaging sub-surface objects by seismic P-wave tomography: Numerical and experimental validations; *Near Surf. Geophys.* **4** 279–287.

Griffiths D H and Barker R D 1993 Two dimensional resistivity imaging and modelling in areas of complex geology; *J. Appl. Geophys.* **29** 211–226.

Günter T, Martin T and Rücker C 2016 Spectral inversion of SIP field data using pyGIMLi/BERT; In: *Proceedings of the 4th International Workshop on Induced Polarization*, Aarhus (Denmark), June 6–8, 2016.

Günther T and Rücker C 2022 Boundless electrical resistivity tomography BERT2 – The User Tutorial; 2019, http://www.resistivity.net/download/bert-tutorial.pdf.

Günther T, Rücker C and Spitzer K 2006 3-d modeling and inversion of DC resistivity data incorporating topography – Part II: Inversion; *Geophys. J. Int.* **166(2)** 506–517.

Hasan M, Shang Y, Jin W and Akhter G 2020 An engineering site investigation using non-invasive geophysical approach; *Environ. Earth Sci.* **79**(**11**), https://doi.org/10.1007/s12665-020-09013-3.

Ivanov J, Miller R D and Peterie S L 2016 Detecting and delineating voids and mines using surface-wave methods in Galena, Kansas; SEG Technical Program Expanded Abstracts 2016, https://doi.org/10.1190/segam2016-13967007.1.

Kang M S, Kim N, Im S B, Lee J J and An Y K 2019 3D GPR Image-based UcNet for enhancing underground cavity detectability; *Remote Sens.* **11** 2545, https://doi.org/10.3390/rs11212545.

Karriqi A and Alikaj P 2011 Combination of resistivity "real section" with quantitative interpretation of vertical electrical soundings; *Proceedings of GeoAlb 2011 "Mineral Resources and Their Perspective"*, Mitrovice, Kosovo, 27–30 September, 2011, pp. 466–469.

Kearey P, Brooks M and Hill I 2013 *An introduction to geophysical exploration*; 3rd edn, Wiley-Blackwell, Oxford, UK, 272p.

Kumar P, Tiwari P, Singh A, Biswas A and Acharya T 2021 Electrical resistivity and induced polarization signatures to delineate the near-surface aquifers contaminated with seawater invasion in Digha, West-Bengal, India; *Catena* **207** 105596, https://doi.org/10.1016/j.catena.2021.105596.

Kumar P, Tiwari P, Biswas A and Acharya T 2022 Geophysical investigation for seawater intrusion in the high-quality coastal aquifers of India: A review; *Environ. Sci. Pollut. Res.*, https://doi.org/10.1007/s11356-022-24233-9.

Leucci G and De Giorgi L 2010 Microgravimetric and ground penetrating radar geophysical methods to map the shallow karstic cavities network in a coastal area (Marina di Capilungo, Lecce, Italy); *Explor. Geophys.* **41** 178–188.

Loke M H 1999 A practical guide to 2D and 3D surveys; Electrical Imaging Surveys for Environmental and Engineering Studies, pp. 1–10.

Loke M H and Barker R D 1996 Rapid least-squares inversion of apparent resistivity pseudosections using a quasi-Newton method; *Geophys. Prospect.* **44** 131–152.

Martínez-Pagán P, Gómez-Ortiz D, Martín-Crespo T, Manteca J I and Rosique M 2013 The electrical resistivity tomography method in the detection of shallow mining cavities. A case study on the Victoria Cave, Cartagena (SE Spain); *Eng. Geol.* **156** 1–10.

Mehanee S 2022a Simultaneous joint inversion of residual gravity and self potential data measured along profile: Theory, numerical examples and a case study from mineral exploration with cross validation from electromagnetic data; *IEEE Trans. Geosci. Remote Sens.* **60** 1–20, https://doi.org/10.1109/TGRS.2021.3071973.

Mehanee S 2022b A new scheme for gravity data interpretation by a faulted 2-D horizontal thin block: Theory, numerical examples and real data investigation; *IEEE Trans. Geosci. Remote Sens.* **60** 1–14, https://doi.org/10.1109/TGRS.2022.3142628.

Mehanee S and Zhdanov M 1999 Magnetotelluric inversion of blocky geoelectrical structures using the minimum support method; *Presented at the 69th International exposition and meeting,* Society of Exploration Geophysicists (SEG), Houston, Texas, USA.

Mehanee S and Zhdanov M 2002 Two-dimensional magnetotelluric inversion of blocky geoelectrical structures; *J. Geophys. Res. Solid Earth* **107**(**B4**), https://doi.org/10.1029/2001JB000191.

Mehanee S, Golubev N and Zhdanov M 1998 Weighted regularized inversion of magnetotelluric data; *Presented at the 68th International and Meeting,* Society of Exploration Geophysicists (SEG), New Orleans, Louisiana, USA.

Mehanee S, Essa K S and Diab Z E 2021 Magnetic data interpretation using a new R-parameter imaging method with application to mineral exploration; *Nat. Resour. Res.* **30**(**1**), https://doi.org/10.1007/s11053-020-09690-8.

Metwaly M and Al Fouzan F 2013 Application of 2-D geoelectrical resistivity tomography for subsurface cavity detection in the eastern part of Saudi Arabia; *Geosci. Front.* **4(4)** 469–476.

Mooney H M 1980 *Handbook of Engineering Geophysics*; Vol. **2**, Electrical Resistivity; Bison Instruments, Inc., 81p.

Niculescu B M and Andrei G 2019 Using Vertical electrical soundings to characterize seawater intrusions in the southern area of Romanian Black Sea Coastline; *Acta Geophys.* **67(6)** 1845–1863.

Nuzzo L, Leucci G and Negri S 2007 GPR, VES and refraction seismic surveys in the karstic area 'spedicaturo' near Nociglia (Lecce, Italy); *Near Surf. Geophys.* **5(1)** 67–76.

Parasnis D S 1997 *Principles of applied geophysics*; 5th edn, Chapman and Hall, London, pp. 104–176.

Pazdirek O and Blaha V 1996 Examples of resistivity imaging using ME-100 resistivity field acquisition system; In: EAGE 58th conference and technical exhibition extended abstracts, Amsterdam.

Plank Z and Polgár D 2019 Application of the DC resistivity method in urban geological problems of karstic areas; *Near Surf. Geophys.* **15(5)** 547–561.

Putiska R, Kusnirak D, Dostal I, Lacny A, Mojzes A, Hok J, Pasteka R, Krajnak M and Bosansky M 2014 Integrated geophysical and geological investigations of karst structures in Komberek, Slovakia; *J. Cave Karst Stud.* **76(3)** 155–163.

Ronczka M, Rücker C and Günther T 2015 Numerical study of long-electrode electric resistivity tomography – Accuracy, sensitivity, and resolution; *Geophysics* **80(6)** 317–328.

Rücker C, Günther T and Spitzer K 2006 Three-dimensional modelling and inversion of dc resistivity data incorporating topography – I. Modelling; *Geophys. J. Int.* **166** 495–505, https://doi.org/10.1111/j.1365-246X.2006.03011.x.

Rücker C, Günther T and Wagner F M 2017 pyGIMLi: An open-source library for modelling and inversion in geophysics; *Comput. Geosci.* **109** 106–123, https://doi.org/10.1016/j.cageo.2017.07.011.

Takahashi T and Kawase T 1990 Analysis of apparent resistivity in a multi-layer earth structure; *IEEE Trans. Power Deliv.* **5** 604–612.

Taltasse P 1953 Recherches géologiques et hydrogéologiques dans le bassin lacustre de Fès-Meknès; *Notes et Mémoires du Service Géologique, Maroc* **115** 152.

Tarantola A 2005 *Inverse problem theory and methods for model parameters estimation*; 1st edn, The Society for Industrial and Applied Mathematics (SIAM), Cambridge University Press, 352p.

Telford W M, Geldart L P and Sheriff R E 1990 Resistivity methods; In: *Applied Geophysics*; 2nd edn, Cambridge Univ. Press, Cambridge, UK, pp. 353–358.

Tikhonov A N and Arsenin V Y 1977 *Solution of ill-posed problems*; V.H. Winston and Sons, Washington D.C., John Wiley & Sons, New York.

Van Schoor M 2002 Detection of sinkholes using 2D electrical resistivity imaging; *J. Appl. Geophys.* **50** 393–399.

Ward S H 1990a *Geotechnical and environmental geophysics*; Vol. II, Environmental and Groundwater; Investigations in Geophysics Series, Society of Exploration Geophysicists, 352p, https://doi.org/10.1190/1.9781560802785.2.

Ward S H 1990b Geotechnical and Environmental Geophysics; Vol. III, Geotechnical Investigations in Geophysics Series, Society of Exploration Geophysicists, 305p, https://doi.org/10.1190/1.9781560802785.3.

Whiteley J S, Chambers J E, Uhlemann S, Wilkinson P B and Kendall J M 2019 Geophysical monitoring of moisture-induced landslides: A review; *Rev. Geophys.* **57** 106–145.

Zhou W, Beck B F and Adams A L 2002 Effective electrode array in mapping karst hazards in electrical resistivity tomography; *Environ. Geol.* **42** 922–928.

Corresponding editor: Arkoprovo Biswas